# Direct visualization of the quantum vortex lattice structure, oscillations and destabilization in rotating 4He

Charles Peretti, Jérémy Vessaire, Emeric Durozoy, Mathieu Gibert

# Direct visualization of the quantum vortex lattice structure, oscillations and destabilization in rotating $^4$He

**Short Title: A path towards quantum turbulence in rotating $^4$He**

**Authors:** Charles Peretti[1], Jérémy Vessaire[1], Émeric Durozoy[1], Mathieu Gibert[1]*

**Affiliations:**

[1]Univ. Grenoble Alpes, Institut Néel - CNRS UPR2940, 25 rue des Martyrs, BP 166, 38042 Grenoble Cedex 9, France.

*Corresponding author. Email: mathieu.gibert@neel.cnrs.fr

**Abstract:** Quantum vortices are a core element of superfluid dynamics and elusively hold the keys to our understanding of energy dissipation in these systems. Here we show that we are able to visualize these vortices in the canonical and higher symmetry case of a stationary rotating superfluid bucket. Using direct visualization, we quantitatively verify Feynman's rule linking the resulting quantum vortex density to the imposed rotational speed. We make the most of this stable configuration by applying an alternative heat flux aligned with the axis of rotation. Moderate amplitudes led to the observation of collective wave mode propagating along the vortices and high amplitudes led to quantum vortex interactions. When increasing the heat flux, this ensemble of regimes defines a path towards quantum turbulence in rotating $^4$He and sets a baseline to consolidate the descriptions of all quantum-fluids.

**One-Sentence Summary:** Visualization of quantum vortex lattice in stationary, oscillating and interacting states promises insights on superfluid models.

**Main Text:**

## Introduction

To model He II (*1*), one needs to use tools at the frontier between fluid and quantum mechanics. Up to this day, there is no unified theory able to describe the dynamics of He II like the Navier-Stokes equation does for classical viscous fluids. Nonetheless, we can assess that this phase of matter exhibits particular properties, such as the superposition of normal fluid and superfluid (*2*). Additionally, the vorticity of the superfluid is constrained on quantum topological defects introduced by R. Feynman (*3*), called quantum vortices. They are atomically thin lines of macroscopic length, and are prime candidates to directly observe macroscopic objects displaying quantum properties. Quantum mechanics imposes that the circulation of the velocity field around these vortex lines is quantized: $\Gamma \equiv \oint v_s \cdot dl = n\kappa$ where $\kappa \equiv h/m \simeq 9.97 \times 10^{-8}$ m$^2$/s is called the Feynman-Onsager quantum of circulation, $h$ is the Planck constant and $m$ the mass of a helium atom, $v_s$ is the superfluid velocity and $n$ is an integer. The velocity field around such a vortex is $|v_s| = \Gamma/2\pi r$ at distance $r$ from the vortex core. Considering kinetic energy, it is straightforward to demonstrate that the system will favor $n$ vortices with a circulation $\pm 1\kappa$ over a single vortex "carrying" $n$ quanta κ. Quantum vortices are an elementary brick of all quantum-fluid systems, such as Bose-Einstein condensates, neutron stars or superconductors, and the main subject of the present article in superfluid helium.

Experimentally, second sound tweezers (*4–6*), quartz tuning forks (*7*, *8*) and electrons (inside bubbles) (*9*) were extensively used to characterize quantum flows at relatively large scales (above the average intervortex spacing), while vibrating wire experiments gave a measure of the circulation quantization and allowed probing of the lowest Kelvin waves modes (*10*) along individual vortices. More recently, micro-machined sensors such as cantilevers (*11*, *12*) and hotwires (*13*, *14*) allowed to lower the smallest scale accessible experimentally taking advantage of large-scale superfluid experimental facilities (*15*, *16*). To develop further models, Lagrangian probes (moving with the flow) entered the field inspired by classical fluid hydrodynamics (*17*, *18*). Up to now, three families of particles have been used as Lagrangian probes: (a) solid particles at room temperature with a density that matches the fluid density (*19*) (hollow glass sphere) or non-buoyant nanoparticles (*20*), (b) hydrogen (*21*, *22*) or deuterium (*23–25*) flakes and (c) metastable $He_2^*$ molecule (*26*). It is hard to conclude firmly on what the first two kinds of particles are tracking exactly (*27–29*), while the third kind traces the normal fluid component only above 1 K and could be trapped on vortices bellow 0.5 K (*30*). Coming back to solid particles, the seminal work done in the early aughts (*21*) convinced the community that these particles could, under certain conditions, decorate quantum vortices (*31–34*). To confirm this thoroughly, we needed a canonical and reproducible experiment that compares to existent predictions without any adjustable parameters. Inspired by the conceptual ease of experiments conducted in the seventies (*35*), we have designed an experiment able to bring this proof: a He II spinning bucket seeded with solid dihydrogen particles under controlled conditions (*36*).

In this article, we directly visualize the quantum vortex density law with di-hydrogen flakes, we compare it quantitatively and without any adjustable parameter to Feynman's prediction. Their match constitutes our main evidence that the dihydrogen flakes are good tracers of quantum vortices in stationary regimes. The observed vortex lattices are analogous to Abrikosov lattices found in superconductors and Bose-Einstein condensates. Furthermore, we use this spinning superfluid bucket configuration as a well-defined and controlled initial condition to explore wave propagation along quantum vortices and vortex/vortex interaction.

In a spinning superfluid bucket, as demonstrated experimentally in 1979 (*35*), we expect that quantum vortices will form and align with the axis of rotation. Seen from the top, they arrange as a regular array that minimizes the free energy of the system while respecting the quantization of circulation of the superfluid (*37*). This vortex array is characterized by the length scale $\delta$, called the intervortex spacing. To estimate this length scale, it is worth noting that a normal fluid under solid body rotation with an angular velocity $\vec{\Omega}$ has a vorticity equal to $2\vec{\Omega}$ everywhere. Therefore, if the number of quantum vortices per unit area in a plane perpendicular to $\vec{\Omega}$ is $n^* = 2\Omega/\kappa$, the circulation around any contour embracing many vortex lines is the same as the one obtained with the solid body rotation. The Feynman's rule simply follows stating that $\delta \equiv 1/\sqrt{n^*} = \sqrt{\kappa/2\,\Omega}$.

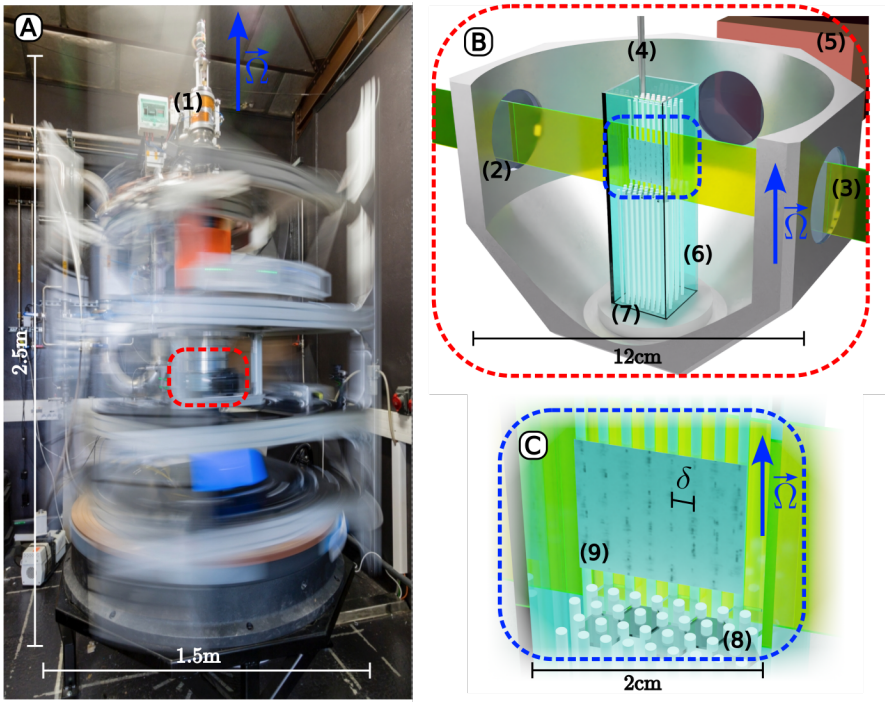


**Figure 1 : Spinning cryostat and measurement scheme.**
Image **A** is a picture of the rotating cryostat, of which the rotary pumping feedthrough (1) is particularly visible as it is static in the laboratory reference frame. Diagram **B** represents a zoomed in slice of the final layer of the experimental cell, which is completely filled with He II during the experiments. It consists of an elongated square cupola with multiple optical ports (2) (transparent to the visible light spectrum) at different angles. Those allow a laser sheet (3) to illuminate a vertical slice of the experimental volume. This laser sheet makes possible the lighting of solid particles of dihydrogen injected via an injection capillary (4) and the capture of their positions with a high-definition camera (S-CMOS with 6 µm pixel size) (5). In order to quell the large-scale flow that arises in the main reservoir and to inject the particles directly in the measurement volume, a 2x2x10 $cm^3$ acrylic glass transparent channel (6) is fixed to the bottom of the experimental cell. Its base (7) also includes a surface heater for further experimentation of the counterflow regime. In the canonical case of constant rotation of the bucket, a vortex array forms inside the channel. Diagram **C** is further zoomed in in order to show the hexagonal array of quantum vortices (8). The white vertical cylinders are a representation of the vortex cores, for better readability, they are not to scale and are sliced horizontally. The experimental photograph (9) is an order of magnitude bigger than reality (here the experimental picture is approximately 1.4 mm wide, axis are equal, whilst the channel is 2 cm wide).

The hexagonal lattice characterized by this length scale $\delta$ is pictured on Figure 1C, and the primary goal of our experiment is to verify the Feynman's rule (or the quantum vortex density law in

rotating $^4$He) that relates directly the rotation rate of the bucket to $\delta$ only through fundamental constants ($\kappa \equiv h/m$).

## Results

### The spinning cryostat

The spinning cryostat that we designed (see Figure 1A) in order to observe this vortex lattice is called CryoLEM for Cryogenic Lagrangian Exploration Module (*38*). The experimental volume has the shape of an elongated square cupola that allows for multiple optical axis orientations when aiming at its center. The heat losses on this entire volume are below 100 mW, thanks to the thermal shield cooled with liquid nitrogen equipped with KG3 windows (*39*). The spinning table main components are two 1.2 m diameter rectified cast-iron plates of about one ton each, see Figure 1A. The first one is stable in the laboratory and the second one levitates on a 50 µm air cushion carrying the spinning cryostat, plus equipment (laser, cameras, sensors and electronics). We use a pressurized air bearing to reduce mechanical vibrations to their lowest limits. On the axis of the table, in the bottom part one can find the drive belt and the electrical feedthrough and, on the top, we have designed in house a rotary pumping feedthrough in order to perpetually control the pressure in the experimental liquid helium reservoir (hence the fluid temperature since we work on a saturated vapor bath). To visualize particles in our experimental volume, we use a 500 mW laser that we extend in one direction using cylindrical lenses arranged in an afocal telescope way.

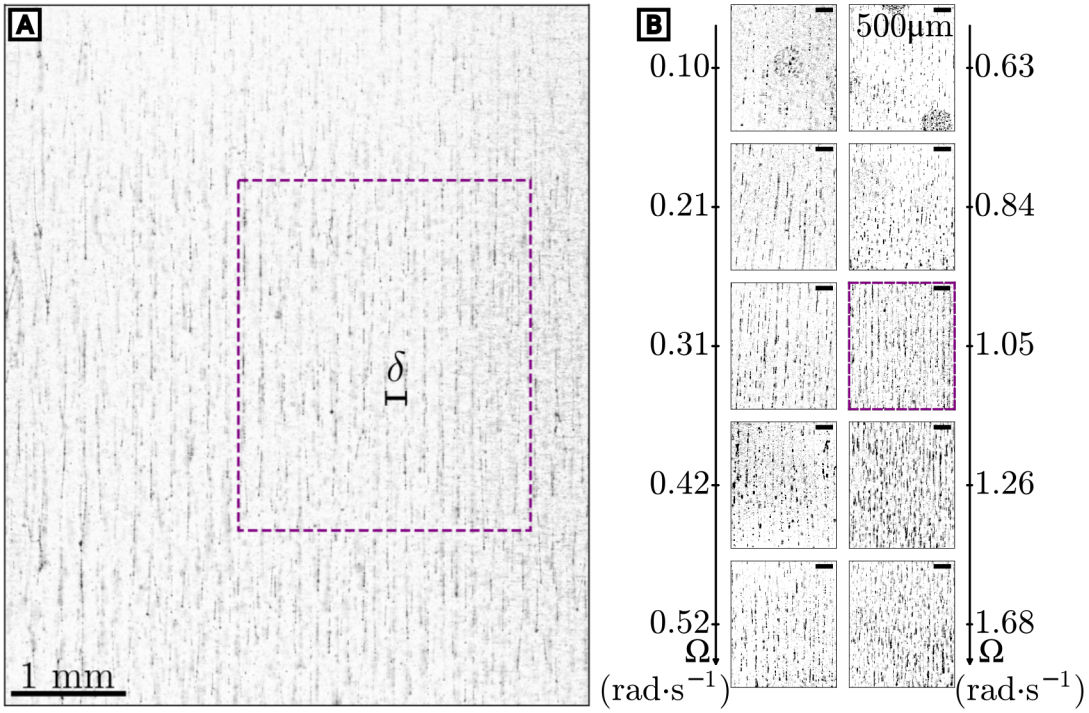


**Figure 2 : Experimental images.**
Inverted images of the region of interest in the rotating cryostat experimental cell. The injected solid dihydrogen particles are in black. The axis of rotation is vertical, aligned with the direction of gravity. Figure **A** is a large-scale image in the center of the channel at $\Omega = 1.047$ rad.s$^{-1}$ (10 RPM). Figure **B** presents images at increasing angular velocity to show the relationship between angular velocity and inter-vortex distance. The purple rectangle in **A** indicates from which zone the $\Omega = 1.047$ rad.s$^{-1}$ (10 RPM) image in **B** is taken from. Horizontal scalebars give the scales of the image **A** and its zoomed-out counterparts **B**.

The light sheet enters the experiment chamber and leaves it through the windows in such a way that the laser beam generates almost no heating on the fluid (liquid helium is transparent to 532nm light and particle density is low). In the middle of the experimental chamber, we have reduced even further the experimental volume by setting up a channel of 2x2 $cm^2$ square cross section and 10 cm high made out of acrylic transparent glass, as depicted in Figure 1B. The role of this channel is primarily to reduce the large-scale flow that arises in the main helium reservoir and to inject the particles directly in the measurement volume. The particles are created thanks to a 98 % helium, 2 % dihydrogen gas mixture at room temperature injected at the top of the channel through a 1.5mm diameter capillary. We have adopted an injection scheme (*21*) detailed in supplementary material Figure S1.

**Measurement of the quantum vortex lattice**

Before starting a new acquisition, the CryoLEM is allowed to spin at the considered rotation rate for about one hour and cooled down to about 2.2 K (just above the transition temperature). We inject the dihydrogen snowflakes and immediately after, start to cool down liquid helium down to $2.160 \pm 0.005$ K (see Figure S1). We trigger the image acquisition when the liquid enters its He II phase. A few seconds after the transition, the turbulence triggered inside the region of interest has decayed and the diffuse cloud of particles seems to "condense" on the vortex lattice, as seen in Figure 2A (borders close to the boundaries were cropped) in which the injected solid di-hydrogen particles are in black. Since we visualize the lattice in a vertical plane that includes the axis of rotation, hydrogen particles appear as series of vertical pearl necklace. This image offers a direct measurement of the intervortex spacing $\delta$ as the distance between two consecutive lines. The distance between vertical lines is reduced when angular velocity increases as seen in Figure 2B. This visually demonstrates the expected consequence of Feynman's rule. The movies that we acquired from these patterns demonstrate a long-duration stability (see Movie S1). We have measured that the particles have an average upward velocity of $v_{settling} = 20 \pm 20$ μm/s that would correspond to particles with a diameter lower than 1 μm if one assumes the viscous Stokes drag with the normal fluid as unique restoring force. As we acquired more than 500 GB of images (~50000 frames), to analyze systematically this dataset, we have developed a technique using a complex Gabor wavelet detailed in the supplementary material. Using this method, we have measured for each experimental condition a series of separation reported on Figure 3 as a function of the rotation rate. The horizontal error bar corresponds to 2% uncertainty of the absolute value of the rotation rate and the vertical one is the dispersion measured by our algorithm (see

supplementary material). On this figure we have also represented the Feynman's rule that has no adjustable parameter and describes properly our data.

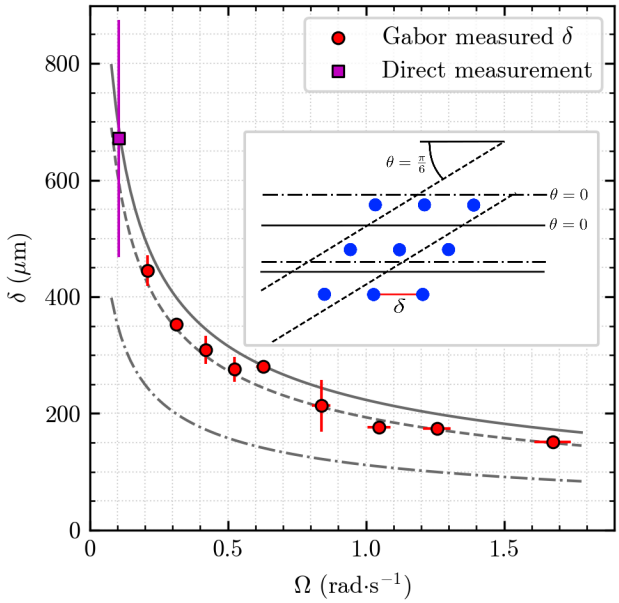


**Figure 3 : Intervortex distance as a function of angular velocity.**
Direct observation of intervortex distance δ in stable vortex arrays at different angular velocity Ω. The measured δ corresponds to the average over multiple images and several films, except for Ω = 1.047 rad.s$^{-1}$ (1 RPM), for which measurements were made manually. Indeed, $\Omega = 1.047 \times 10^{-1}$ rad.s$^{-1}$ (1 RPM) sessions yielded few exploitable images in which the vortex array was homogeneously distributed. The three black lines alongside our data are the expected measurements of δ depending on the relative orientation of the vortex lattice with respect to the camera's field of view. The inset schematically represents this relative orientation using a pair of lines with identical styles materializing the depth of field: when the array and the imaged region are aligned and the depth of field is small enough to capture only one (solid lines) or two (dashed dotted lines) layers of vortices, or when the array and the imaged region are misaligned by π/6 (dashed lines).

## Discussion

The agreement between our measurements and the Feynman's rule over such a large data set analyzed using an objective mathematical approach is the main result of this paper. It demonstrates that direct visualization of quantum vortices via hydrogen flakes can lead to quantitative physical interpretations. Nevertheless, we have to discuss the fact that we have no way to align the imaged region with any of the vectors defining the unit cell of the expected hexagonal vortex lattice. The laser sheet enters the channel orthogonally to its wall and the quantum vortex lattice orients itself inside the channel. The boundary conditions of this canonical problem are such that about one layer of vortex lines is missing close to the border of the container because of the "image" vortex lines contribution to the velocity field. The effect of the square cross section of the channel on our measurement is out of the scope of this paper, but requires further research. Therefore, we are left with the fact that with a depth of field of about 150 μm, we can measure a separation between the exact Feynman's rule value δ if the principal axis of the lattice is colinear with the imaged region and $\delta\, cos(\pi/6)$ if it is misaligned (see

Figure 3 inset). All our data points are indeed in between those two limits. This allows to conclude that we have verified Feynman's rule by direct visualization of hydrogen solid particles trapped on the quantum vortices core. If we recall now that hydrogen flakes have a diameter of order 1 μm and that the quantum vortex core has a diameter of order 1 Å we could compare this situation to a *whale pod attached to a quantum fishing line*. This scale comparison recalls us that these particles may be passive in this particular stationary case as demonstrated by our measurements, but it may not be the case when considering a dynamical case.

Furthermore, this lattice configuration is the perfect initial condition to trigger and study wave propagating along these quantum vortices and vortex/vortex interaction. At the bottom of the channel, we have installed a surface heater that can trigger a normal fluid momentum flux toward the open end of the channel. Below an amplitude of a few mW (out of the scope of this paper), nothing happens. Then when this heater is driven with an alternating current, a collective wave mode is triggered along the vortex lines as shown on Figure 4. Its frequency is the one of the thermal excitations and its transverse amplitude (in horizontal displacement) depends on this frequency and exhibits a resonance when the normal fluid is driven vertically with a frequency equal to the rotation rate Ω. These promising experimental results are here to "feed" different theoretical approaches as they complement the picture drawn by Nuclear Magnetic Resonance on a librating superfluid $^3$He (40). In particular, the initial threshold has to be linked to the Donnelly-

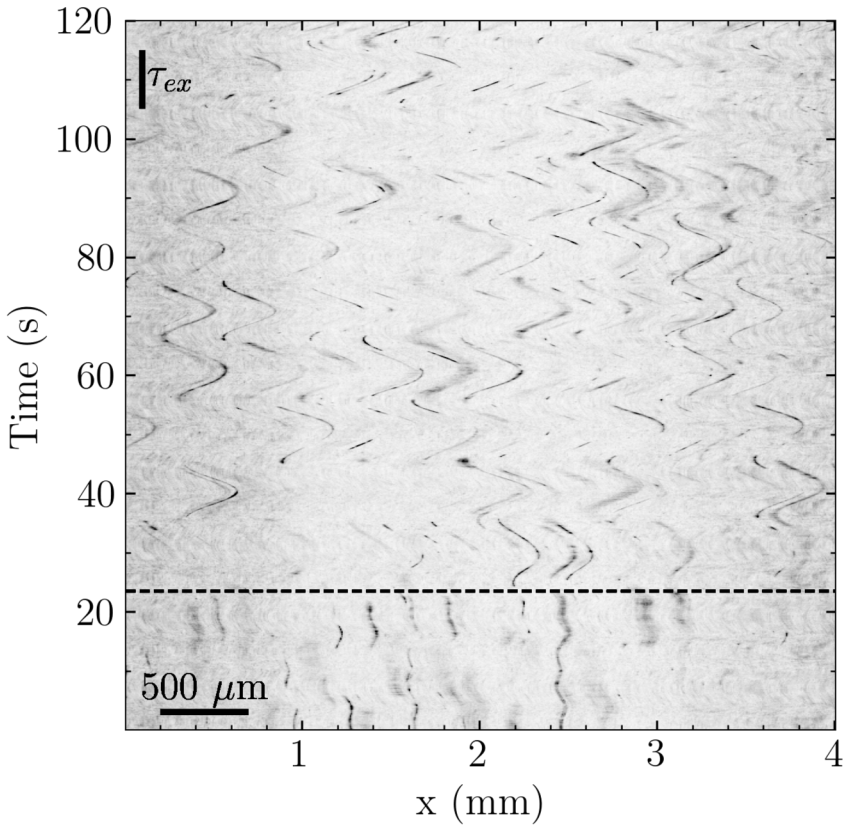


**Figure 4 : Space-time visualization of wave propagation along quantum vortices.**
Space-time representation of a single horizontal line of pixels in an experimental movie at angular velocity $\Omega = 5.236 \times 10^{-1}$ rad.s$^{-1}$ (5 RPM). The horizontal scalebar represents a 500 μm scale, while the vertical scalebar $\tau_{ex}$ represents 10 s. The horizontal dotted line indicates the time $t_0$ after which the heater is activated with a periodic positive square function of period $\tau_{ex}$, and of heating power 3.6 mW over a period (9 W.m$^{-2}$). Although there exists periodic horizontal movement before $t_0$, the heat injection after $t_0$ generates ample periodic horizontal motion coming from the wave propagation along the vortices.

Glaberson (*41*) instability, and the waves triggered on the lattice can be inertial (*42*), Kelvin or Tkachenko waves depending on the regime considered (*43,44*). A thorough comparison between these experimental results and theoretical approaches (*45*) could lead to a proper description of the particle/vortex interaction and a better understanding of the value of the coefficients in Schwarz's equation (*46*).

When the heater power is pushed even further, case considered in Movie S2, the quantum vortex lines start to "see" each other up to a point where they interact strongly and trigger thousands of interactions in between neighbouring vortices of the initial vortex lattice and *in fine* destroy it. The flow evolves toward a spinning counter flow state (*47*). This opens a way to study the reconnection process between quantum vortices, systematically, from a well-known and established initial condition, while controlling the driving force. These reconnexions are expected to play a key role in the energy dissipation processes at ultra-low temperature but also in the establishment of the quantum vortex lattice (*48*). To analyze these dynamical results further, a direct comparison with numerical simulations based on a model that fully couples the vortex line dynamics with the normal fluid, such as the recently developed FOUCAULT (*49*) model, is needed to account for finite temperature effects.

In summary, through the use of a Gabor wavelet, we show that the spatial distribution of di-hydrogen flakes seeding a spinning He II bucket follows the Feynman's rule. Therefore, we experimentally demonstrated that di-hydrogen flakes are good tracers of quantum vortices in He II in stationary cases. This enables us to build reproducible and controlled initial conditions for further dynamical studies of quantum vortices. Additionally, we explore the effect of a surface heater driven by an alternating current at the bottom of our experimental channel. We've identified that below a certain threshold the vortex lattice remains unperturbed, and above a collective wave mode arises. Preliminary results tend to prove that the amplitude of these waves is maximal when heat flux frequency equals to the rotation rate of the experiment. When pushing the heat flux further, neighbor vortices start to see each other and interact. This opens a way to study quantum vortex reconnexion while controlling their initial condition and the driving force that triggers these extreme events. Both dynamical cases introduced here deserve further research that should lead to a better understanding of the physics of quantum vortices and ultimately improve superfluid models thanks to direct visualization of this macroscopic quantum object in He II.

## Materials and Methods

Temperature control and particle injection scheme

The temperature of the experimental liquid helium ($T_{cell}$) is continuously controlled by controlling the pressure of the cell ($P_{cell}$). To do so, we take advantage of a homemade leak-tight rotating gaseous feedthrough connected to a 300$m^3$/h vacuum pump through a manifold that allows many types of regulations. The main component that we use in these experiments is a diaphragm pressure regulator (throughput 50$m^3$/h) which is an absolute pressure regulator which automatically adapts the pumping speed of the vacuum pump depending on the amount of He that evaporates from the cryostat. The pressure setpoint is given by the pressure inside a reference chamber that we monitor at all times ($P_{regulator}$). The pressure difference ($P_{regulator}$ - $P_{cell}$) is calibrated beforehand and presents a slow drift in time when the stationary state is reached during experimental sessions (maximum temperature drift of 0.7% for a 20-minute session). To generate the particles that we observe, we inject a gaseous mixture of 98% of He and 2% of $H_2$ at room temperature directly into the experimental cell through a 1m long and 1.5mm inner diameter cupro-nickel capillary tube. The gas mixture is embedded on the spinning table and newly prepared every day in a 1L reservoir

filled at 3.5 bars. To ensure full control over the process, hence repeatability, we have positioned a high-precision single-stage absolute pressure regulator (tied-diaphragm regulator) that sets $P_{injection}$ on the cupro-nickel capillary tube as close as possible to the entrance into the cryostat's core. This way, we control the end-to-end pressure difference on the injection tube regardless the pressure in the reservoirs (3.5 bars for the first experiment but it decreases injection after injection). The pressure difference ($P_{injection}$ - $P_{cell}$) naturally sets the flow rate inside the injection capillary tube. Figure S1 shows a typical measurement run. This entire sequence is done under a constant rotation speed. After the first cool down below $T_\lambda$ (lambda point temperature), we bypass the pressure regulation, the temperature rises above the transition, then we inject the particles, trigger the image acquisition and close the bypass of the diaphragm pressure regulator to decrease the temperature. When the fluid transits to its He II phase, the cloud of particles "condenses" onto the vortex lattice. Because solid $H_2$ is less dense ($\rho_{H2}$=88kg/m$^3$) than liquid He ($\rho_{He}$=145kg/m$^3$), particles tend to move upwards, out of our region of interest and out of the channel. Therefore, we repeat the cycle described above in order to acquire more data.

Gabor wavelet analysis

To get reliable and trustworthy results, we have conducted many experimental runs. Precisely, we have acquired 500 GB of images which corresponds to about 50000 frames. To analyze this amount of data, we developed an algorithm based on the 2D Gabor wavelet, using Python3 and the OpenCV library. The algorithm was implemented in an embarrassingly parallel manner.

The Gabor wavelet is a 2D Gaussian modulated by a complex exponential. We used a simplified form represented on Figure S2 and defined as followed:

$$G(x,y) = e^{\frac{-(x^2+y^2)}{2\sigma^2}} e^{j\frac{2\pi x}{\lambda}}$$

This expression unveils 3 length scales ordered increasingly: σ defining the Gaussian width, λ defining the probed wavelength, and implicitly L the size of kernel. We have chosen the following relations to link them:

$$\begin{cases} \sigma = \lambda/2 \\ L = 1 + 2 \times ceil(4\sigma) \end{cases}$$

This definition allows us to consider that G(x,y) has only one parameter λ. We have simplified the most general form of the Gabor wavelet to respect the vertical invariance and horizontal periodicity of the images that we probe. We use this complex function as a kernel of convolution with our images to compute the amplitude of this correlation at any given point of all our images for many wavelength λ. Then we study the sum of these amplitudes over all the pixels of a given image that we call intensity and we study this intensity as a function of λ. Figure S3 is here to grasp qualitatively what should we expect from such an image analysis process. The perfect match between the maxima of the kernel and the one of the images in the $\lambda_{gabor} = \lambda_{image}$ case let us conclude that the correlation should be maximum in that case. On the contrary, when $\lambda_{gabor} = 2\lambda_{image}$ the first minima of the kernel fall into a maximum of the probed pattern, one can expect that this negative contribution will annihilate the positive one due to the central pic at order zero. Finally, when $\lambda_{gabor} = \lambda_{image}/2$, the secondary maxima of the kernel match with local maxima of the image, therefore we should observe a secondary maximum in the amplitude of the correlation. We do this computation in the complex domain in order to get rid of any phase when computing the amplitude of the complex correlation. Moreover, the vertical invariance that we have chosen for the kernel is here to deal with the fact that our images are not as perfect as the synthetic one showed on Figure S3. Indeed, as seen on Figure 2, the quantum vortices are decorated by irregular

point particles. Having a finite vertical extension let the wavelet average the image over a length scale larger than the particles size, which allows particles at different heights to be considered together when looking for a horizontally periodic pattern. When computing on an experimental image, we get S4 (top). One needs to normalize the correlation by the weight of the kernel proportional to $\lambda^2$, that gives the spectrum S4 (bottom). We have run several tests on many synthetic images (introducing fake particles and noise) and they all clearly confirm that the second peak corresponds to the periodicity of the pattern. Surprisingly, the first peak after normalization turns out to have a higher normalized intensity. This is because we have not considered in our qualitative analysis that when $\lambda_{gabor}/2$ approaches the particle size, this should show up in the spectrum. After running a collection of different tests, we can conclude that this first peak is a mixture of $\lambda_{gabor} = \lambda_{image}/2$ , $\lambda_{gabor}/5 \cong$ particle size and the particle number density in the image. As our goal is to measure the horizontal periodicity of our images in order to get access to the intervortex distance, we do not push our analysis of the first peak any further. If we were to measure apparent particle size, we would use other methods. We have run this analysis on all our images. Using a bimodal fit on each normalized intensity recovered for each frame, we are able to measure the intervortex distance as a function of time with a subpixel resolution. Figure S5, shows the result of this temporal analysis of a given movie in the 5RPM batch. This representation helps us define when the stationary state is reached and to compute the average and standard deviation of our intervortex spacing measurement. We used this standard deviation alongside the bimodal fit standard deviation to define the vertical error bars in Figure 3.

## References and Notes

1. R. J. Donnelly, *Experimental Superfluidity* (The University of Chicago Press, 1967).
2. R. J. Donnelly, *Quantized Vortices in Helium II* (Cambridge University Press, 1991).
3. R. P. Feynman, Applications of quantum mechanics to liquid helium. *Prog. Low Temp. Phys.* **1**, 17–53 (1955).
4. S. Babuin, M. Stammeier, E. Varga, M. Rotter, L. Skrbek, Quantum turbulence of bellows-driven $^4$He superflow: Steady state. *Phys. Rev. B*. **86** (2012), doi:10.1103/physrevb.86.134515.
5. E. Varga, S. Babuin, L. Skrbek, Second-sound studies of coflow and counterflow of superfluid $^4$He in channels. *Phys. Fluids*. **27**, 65101 (2015).
6. E. Woillez, J. Valentin, P. E. Roche, Local measurement of vortex statistics in quantum turbulence. *Epl*. **134**, 1–7 (2021).
7. D. Duda, thesis, Universitas Carolina Facultas Mathematica Physicaque (2017).
8. D. Schmoranzer, M. J. Jackson, V. Tsepelin, M. Poole, A. J. Woods, M. Človečko, and L. Skrbek, Multiple critical velocities in oscillatory flow of superfluid $^4$He due to quartz tuning forks. *Phys. Rev. B*, **94**, 214503 (2016).
9. P. M. Walmsley, A. I. Golov, Quantum and quasiclassical types of superfluid turbulence. *Phys. Rev. Lett.* **100**, 8–11 (2008).
10. R. J. Zieve, Sixty Years of Quantized Circulation, *Journal of Low Temperature Physics* (2023), https://doi.org/10.1007/s10909-023-02956-4.
11. J. Salort, É. Rusaouën, L. Robert, R. Du Puits, A. Loesch, O. Pirotte, P. E. Roche, B. Castaing, F. Chillà, A local sensor for joint temperature and velocity measurements in turbulent flows. *Rev. Sci. Instrum.* **89**, 1–12 (2018).
12. J. Salort, F. Chill, E. Rusaouën, P. E. Roche, M. Gibert, I. Moukharski, A. Braslau, F. Daviaud, B. Gallet, E. W. Saw, B. Dubrulle, P. Diribarne, B. Rousset, M. B. Mardion, J. P. Moro, A. Girard, C. Baudet, V. L'Vov, A. Golov, S. Nazarenko, Experimental signature of quantum turbulence in velocity spectra? *New J. Phys.* **23**, 1–16 (2021).

13. P. Diribarne, P. Thibault, P. E. Roche, Nano-shaped hot-wire for ultra-high resolution anemometry in cryogenic helium. *Rev. Sci. Instrum.* **90**, 1–8 (2019).
14. P. Diribarne, M. Bon Mardion, A. Girard, J. P. Moro, B. Rousset, F. Chilla, J. Salort, A. Braslau, F. Daviaud, B. Dubrulle, B. Gallet, I. Moukharski, E. W. Saw, C. Baudet, M. Gibert, P. E. Roche, E. Rusaouen, A. Golov, V. L'Vov, S. Nazarenko, Investigation of properties of superfluid $^4$He turbulence using a hot-wire signal. *Phys. Rev. Fluids*. **6**, 1–16 (2021).
15. B. Rousset, P. Bonnay, P. Diribarne, A. Girard, J. M. Poncet, E. Herbert, J. Salort, C. Baudet, B. Castaing, L. Chevillard, F. Daviaud, B. Dubrulle, Y. Gagne, M. Gibert, B. Hébral, T. Lehner, P.-E. Roche, B. Saint-Michel, M. B. Mardion, Superfluid High REynolds von Kármán experiment. *Rev. Sci. Instrum.* **85**, 103908 (2014).
16. B. Saint-Michel, E. Herbert, J. Salort, C. Baudet, M. B. Mardion, P. Bonnay, M. Bourgoin, B. Castaing, L. Chevillard, F. Daviaud, P. Diribarne, B. Dubrulle, Y. Gagne, M. Gibert, A. Girard, B. Hébral, T. Lehner, B. Rousset, Probing quantum and classical turbulence analogy in von Kármán liquid helium, nitrogen, and water experiments. *Phys. Fluids*. **26**, 125109 (2014).
17. N. Mordant, E. Lévêque, J.-F. ccois Pinton, Experimental and numerical study of the Lagrangian dynamics of high Reynolds turbulence. *New J. Phys.* **6**, 116-+ (2004).
18. N. Mordant, A. M. Crawford, E. Bodenschatz, Experimental lagrangian acceleration probability density function measurement. *Phys. D-Nonlinear Phenom.* **193**, 245–251 (2004).
19. F. Sy, P. Diribarne, B. Rousset, M. Gibert, M. Bourgoin, Multiscale energy budget of inertially driven turbulence in normal and superfluid helium. *Phys. Rev. Fluids*. **6**, 1–24 (2021).
20. Y. Minowa, S. Aoyagi, S. Inui, T. Nakagawa, G. Asaka, M. Tsubota, M. Ashida, Visualization of quantized vortex reconnection enabled by laser ablation. *Sci. Adv.* **8** (2022), doi:10.1126/sciadv.abn1143.
21. G. P. Bewley, thesis, Yale University (2006).
22. G. P. Bewley, K. R. Sreenivasan, D. P. Lathrop, Particles for tracing turbulent liquid helium. *Exp. Fluids*. **44**, 887–896 (2007).
23. M. La Mantia, D. Duda, M. Rotter, L. Skrbek, Lagrangian accelerations of particles in superfluid turbulence. *J. Fluid Mech.* **717** (2013), doi:10.1017/jfm.2013.31.
24. P. Švančara, M. La Mantia, Flows of liquid $^4$He due to oscillating grids. *J. Fluid Mech.* **832**, 578–599 (2017).
25. P. Hrubcová, P. Švančara, M. La Mantia, Vorticity enhancement in thermal counterflow of superfluid helium. *Phys. Rev. B*. **97** (2018), doi:10.1103/physrevb.97.064512.
26. W. Guo, S. B. Cahn, J. A. Nikkel, W. F. Vinen, D. N. McKinsey, Visualization study of counterflow in superfluid {$^4He$} using metastable helium molecules. *Phys. Rev. Lett.* **105** (2010), doi:10.1103/physrevlett.105.045301.
27. P. Švančara, D. Duda, P. Hrubcová, M. Rotter, L. Skrbek, M. La Mantia, E. Durozoy, P. Diribarne, B. Rousset, M. Bourgoin, M. Gibert, Ubiquity of particle-vortex interactions in turbulent counterflow of superfluid helium. *J. Fluid Mech.* **911**, 1–22 (2021).
28. B. Mastracci, W. Guo, An apparatus for generation and quantitative measurement of homogeneous isotropic turbulence in He II. *Rev. Sci. Instrum.* **89**, 15107 (2018).
29. N. Sakaki, T. Maruyama, Y. Tsuji, Study on the Curvature of Lagrangian Trajectories in Thermal Counterflow. *J. Low Temp. Phys.* (2022), doi:10.1007/s10909-022-02734-8.
30. D. E. Zmeev, F. Pakpour, P. M. Walmsley, A. I. Golov, W. Guo, D. N. McKinsey, G. G. Ihas, P. V. E. McClintock, S. N. Fisher, W. F. Vinen, Excimers He2* as tracers of

quantum turbulence in He4 in the T=0 Limit. *Phys. Rev. Lett.* **110**, 1–5 (2013).
31. G. P. Bewley, D. P. Lathrop, K. R. Sreenivasan, Visualization of quantized vortices. *Nature*. **441**, 588 (2006).
32. E. Fonda, K. R. Sreenivasan, D. P. Lathrop, Sub-micron solid air tracers for quantum vortices and liquid helium flows. *Rev. Sci. Instrum.* **87**, 25106 (2016).
33. G. P. Bewley, M. S. Paoletti, K. R. Sreenivasan, D. P. Lathrop, Characterization of reconnecting vortices in superfluid helium. *Proc. Natl. Acad. Sci. U. S. A.* **105**, 13707–13710 (2008).
34. G. P. Bewley, The generation of particles to observe quantized vortex dynamics in superfluid helium. *Cryogenics (Guildf).* **49**, 549–553 (2009).
35. E. J. Yarmchuk, M. J. V Gordon, R. E. Packard, Observation of stationary vortex arrays in rotating superfluid helium. *Phys. Rev. Lett.* **43**, 214–217 (1979).
36. E. Durozoy, thesis, Université Grenoble Alpes (2020).
37. H. E. Hall, The rotation of liquid helium II. *Adv. Phys.* **9**, 89–146 (1960).
38. R. Zimmermann, H. Xu, Y. Gasteuil, M. Bourgoin, R. Volk, J.-F. Pinton, E. Bodenschatz, The Lagrangian exploration module: An apparatus for the study of statistically homogeneous and isotropic turbulence. *Rev. Sci. Instrum.* **81**, 5112 (2010).
39. M. Melich, R. Boltnev, F. Bonnet, L. Guyon, P. E. Wolf, On the efficiency of infrared filters in optical cryostats. *J. Low Temp. Phys.* **162**, 740–747 (2011).
40. J. T. Mäkinen, S. Autti, P. J. Heikkinen, J. J. Hosio, R. Hänninen, V. S. L'vov, P. M. Walmsley, V. V. Zavjalov, V. B. Eltsov, Rotating quantum wave turbulence. *Nat. Phys.* (2023). https://doi.org/10.1038/s41567-023-01966-z
41. W. I. Glaberson, W. W. Johnson, R. M. Ostermeier, Instability of a vortex array in{ He II}. *Phys. Rev. Lett.* **33**, 1197–1200 (1974).
42. D. O. Mora, E. Monsalve, M. Brunet, T. Dauxois, P. P. Cortet, Three-dimensionality of the triadic resonance instability of a plane inertial wave. *Phys. Rev. Fluids*. **6**, 1–27 (2021).
43. E. B. Sonin, Tkachenko waves. *{JETP} Lett.* **98**, 758–768 (2014).
44. K. L. Henderson, C. F. Barenghi, Vortex waves in a rotating superfluid. *EPL* **67** 56 (2004).
45. R. A. Van Gorder, The Biot-Savart description of Kelvin waves on a quantum vortex filament in the presence of mutual friction and a driving fluid. *Proc. R. Soc. A Math. Phys. Eng. Sci.* **471** (2015), doi:10.1098/rspa.2015.0149.
46. K. W. Schwarz, Three-dimensional vortex dynamics in superfluid He4: Line-line and line-boundary interactions. *Phys. Rev. B*. **31**, 5782–5804 (1985).
47. C. E. Swanson, C. F. Barenghi, R. J. Donnelly, Rotation of a tangle of quantized vortex lines in {He II}. *Phys. Rev. Lett.* **50**, 190–193 (1983).
48. N. A. Keepfer, G. W. Stagg, L. Galantucci, C. F. Barenghi, N. G. Parker, Spin-up of a superfluid vortex lattice driven by rough boundaries. *Phys. Rev. B*. **102**, 1–11 (2020).
49. L. Galantucci, A. W. Baggaley, C. F. Barenghi, G. Krstulovic, A new self-consistent approach of quantum turbulence in superfluid helium. *Eur. Phys. J. Plus*. **135**, 1–28 (2020).

**Acknowledgments:** We thank G. Garde for his deep implication in the project as lead engineer, his contribution to this work is crucial. We acknowledge P. Spathis , B. Chabaud and O. Bourgeois for insightful discussions all along the project.

**Funding:** This work received the support of grants:

ANR-11-PDOC-0001 (3D-QuantumV)

ANR-10-LABX-0051 (LANEF)

ANR-17-CE30-0003 (DisET)

**Author contributions:** All authors significantly contributed to this work as a team effort. M.G. carries out the project since the beginning (2011).

Conceptualization: MG

Methodology: CP, JV, ED, MG

Investigation: CP, JV, MG

Visualization: CP, JV, MG

Funding acquisition: MG

Project administration: MG

Supervision: MG

Writing – original draft: MG, CP

Writing – review & editing: CP, JV, ED, MG

**Competing interests:** Authors declare that they have no competing interests.

**Data and materials availability:** All data needed to evaluate the conclusions in the paper are present in the paper and/or the Supplementary Materials.

## Supplementary Materials

Figs. S1 to S5

Table S1

Movies S1 to S2